nature structural & molecular biology

Axin cancer mutants form nanoaggregates to rewire the Wnt signaling network

Zeinab Anvarian[1,11], Hisashi Nojima[2,11], Eline C van Kappel[1,11], Tobias Madl[3–6], Maureen Spit[1], Martin Viertler[4], Ingrid Jordens[1], Teck Y Low[7,8], Revina C van Scherpenzeel[1], Ineke Kuper[1], Klaus Richter[9], Albert J R Heck[7,8], Rolf Boelens[3], Jean-Paul Vincent[2], Stefan G D Rüdiger[10] & Madelon M Maurice[1]

Signaling cascades depend on scaffold proteins that regulate the assembly of multiprotein complexes. Missense mutations in scaffold proteins are frequent in human cancer, but their relevance and mode of action are poorly understood. Here we show that cancer point mutations in the scaffold protein Axin derail Wnt signaling and promote tumor growth *in vivo* through a gain-of-function mechanism. The effect is conserved for both the human and *Drosophila* proteins. Mutated Axin forms nonamyloid nanometer-scale aggregates decorated with disordered tentacles, which 'rewire' the Axin interactome. Importantly, the tumor-suppressor activity of both the human and *Drosophila* Axin cancer mutants is rescued by preventing aggregation of a single nonconserved segment. Our findings establish a new paradigm for misregulation of signaling in cancer and show that targeting aggregation-prone stretches in mutated scaffolds holds attractive potential for cancer treatment.

Scaffold proteins orchestrate the formation and activity of multiprotein complexes and thereby control the flow of cellular information[1]. These proteins typically combine compact folded domains with large intrinsically disordered segments, which mediate highly specific but low-affinity interactions with multiple binding partners[2–6]. Misregulation of these signaling hubs is frequent in cancer, as exemplified by the large number of germline and somatic mutations in tumor-suppressor scaffolds, such as BRCA1, APC and Axin[6–9]. A major fraction of these mutations comprises single point mutations with poorly understood functional implications. Basic insight into these mutants' molecular modes of action is of fundamental importance to define common principles by which mutagenic events drive carcinogenesis, to distinguish driver from passenger mutations and to provide prognostic information and guide therapeutic decisions.

Here we set out to identify driver mutations in the *AXIN1* gene product, Axin, a critical tumor suppressor of Wnt signaling, and to uncover the mechanism by which these mutations cause oncogenesis. The primary role of Axin (**Fig. 1a**) is to scaffold a multiprotein destruction complex, which drives the phosphorylation and subsequent proteolysis of the transcriptional regulator β-catenin[10–13]. In healthy cells, Wnt-mediated signals inhibit destruction-complex activity toward β-catenin, thus leading to β-catenin accumulation, nuclear entry and transcriptional activation of target genes involved in tissue self-renewal and growth[14–16]. Accordingly, aberrant activation of β-catenin due to mutations in destruction-complex components is frequently linked to the development of human cancer[16]. Restoration of normal Wnt-pathway regulation at late cancer stages can revert colorectal cancer cells into functioning normal cells, thus validating the Wnt pathway as an effective therapeutic target[17].

Axin mutations are associated with a diverse set of tumors including hepatocellular, colorectal and endometrial carcinoma, melanoma and stomach adenocarcinoma (http://www.cbioportal.org/). Strikingly, the mutational spectrum in Axin shows a higher prevalence of missense mutations than deletions and truncations, and missense mutations are frequently accompanied by a gain in copy number and mRNA overexpression, thus suggesting a selective advantage of point-mutant protein expression in tumor development (http://cancer.sanger.ac.uk/cosmic/gene/overview?ln=AXIN1). However, how the poorly classified class of Axin point mutants may contribute to tumorigenesis remains unknown.

Using a multiscale approach, including structural studies and whole-animal assays, we uncovered a molecular mechanism by which missense mutations convert signaling hubs into protumorigenic proteins. We show that tumor growth–promoting cancer mutations in Axin destroy the conserved core of the N-terminal Axin RGS domain. The destabilized protein gains new properties by forming soluble nanometer-scale aggregates of at least 4 or 5 molecules. Nonaggregating, natively disordered regions of Axin protrude from the oligomer as molecular

[1]Department of Cell Biology, Center for Molecular Medicine, University Medical Center Utrecht, Utrecht, the Netherlands. [2]The Francis Crick Institute, Mill Hill, London, UK. [3]NMR Spectroscopy Research Group, Bijvoet Center for Biomolecular Research, Utrecht University, Utrecht, the Netherlands. [4]Institute of Structural Biology, Helmholtz Zentrum München, Neuherberg, Germany and Biomolecular NMR spectroscopy, Technische Universität München, Garching, Germany. [5]Institute of Molecular Biology and Biochemistry, Medical University of Graz, Graz, Austria. [6]Omics Center Graz, BioTechMed Graz, Graz, Austria. [7]Biomolecular Mass Spectrometry and Proteomics, Bijvoet Center for Biomolecular Research and Utrecht Institute for Pharmaceutical Sciences, Utrecht University, Utrecht, the Netherlands. [8]The Netherlands Proteomics Center, Utrecht, the Netherlands. [9]Department of Chemistry, Technische Universität München, Garching, Germany. [10]Cellular Protein Chemistry, Bijvoet Centre for Biomolecular Research, Utrecht University, Utrecht, the Netherlands. [11]These authors contributed equally to this work. Correspondence should be addressed to S.G.D.R. (s.g.d.rudiger@uu.nl) or M.M.M. (m.m.maurice@umcutrecht.nl).

Received 17 July 2015; accepted 12 February 2016; published online 14 March 2016; doi:10.1038/nsmb.3191

tentacles that aberrantly engage key regulators. As a consequence, the Axin signaling network is rewired to allow activation of β-catenin–mediated transcription. Importantly, blocking aggregation is sufficient to rescue tumor-suppressor activity of the mutant protein *in vivo*, whereas refolding of the damaged domain is not required. We propose that conformational conversion into nonamyloid, single-domain nanoaggregates constitutes a general gain-of-function mechanism for cancer mutations that destabilize signaling scaffolds.

RESULTS

Axin cancer point mutants fail to suppress Wnt signaling

Axin comprises an N-terminal RGS domain and a C-terminal oligomerizing DIX domain, both of which are connected by a natively disordered central region[4,18,19] (**Fig. 1a**). The RGS domain, which mediates the interaction of Axin with the tumor suppressor APC, is affected by several cancer mutations[8,18]. To assess how alterations in the RGS domain contribute to tumor growth, we analyzed a set of six point mutants in conserved RGS residues identified in human cancers[20–23] (**Fig. 1b** and **Supplementary Fig. 1a**). We expressed these Axin variants in HEK293T cells and compared their activity in a β-catenin–dependent luciferase reporter assay (**Fig. 1c**,**d**). We expected expression of functional Axin to suppress both background and Wnt-induced signaling. Indeed, we observed suppression of signaling for wild-type (WT) Axin and two mutants (Axin T122A and Axin S215L). In contrast, a subset of mutants markedly failed to inhibit β-catenin–mediated transcription. This was particularly striking for both Axin L101P and Axin L106R, which triggered strong signaling even in the absence of exogenous Wnt (**Fig. 1c**). Therefore, these RGS variants, through an unknown molecular mechanism, are likely to interfere with β-catenin degradation.

Cancer mutations destabilize the Axin RGS domain

To elucidate the mechanism underlying the effects of the RGS variants, we mapped the mutants onto the structure of the RGS domain. Remarkably, none of the six cancer-associated mutations mapped to the conserved APC-binding groove (**Fig. 1e**). The two mutations with the strongest effects occurred at buried residues, which are unable to directly interact with any potential Axin-binding partners: RGS L106R, which affects the architecture of the hydrophobic core, and RGS L101P, which alters the polypeptide backbone. We therefore asked whether tumorigenic RGS mutations might impair Axin function through long-range allosteric effects. Fluorescence-based thermal denaturation showed that RGS WT, RGS T122A and RGS S215L unfolded at similar temperatures (53–55 °C), thus indicating their structural integrity (**Fig. 1f**). Strikingly, the functionally defective RGS R103M, RGS K203M and RGS L101P were substantially less stable (unfolding at 44–48 °C), and RGS L106R was even more destabilized (unfolding at 27 °C). Unfolding of all Axin RGS variants was accompanied by a loss of helical structure, as measured by circular dichroism spectroscopy (**Supplementary Fig. 1b**). The highly destabilized RGS L106R mutant entirely lost α-helical propensity far below physiological temperature. Overall, the extent of destabilization significantly correlated with an inability to suppress β-catenin–mediated transcription (**Fig. 1g**; $r = -0.97$ and $P = 0.0003$). We conclude that the failure of cancer mutants to suppress β-catenin signaling is tightly coupled to the loss of RGS structural stability.

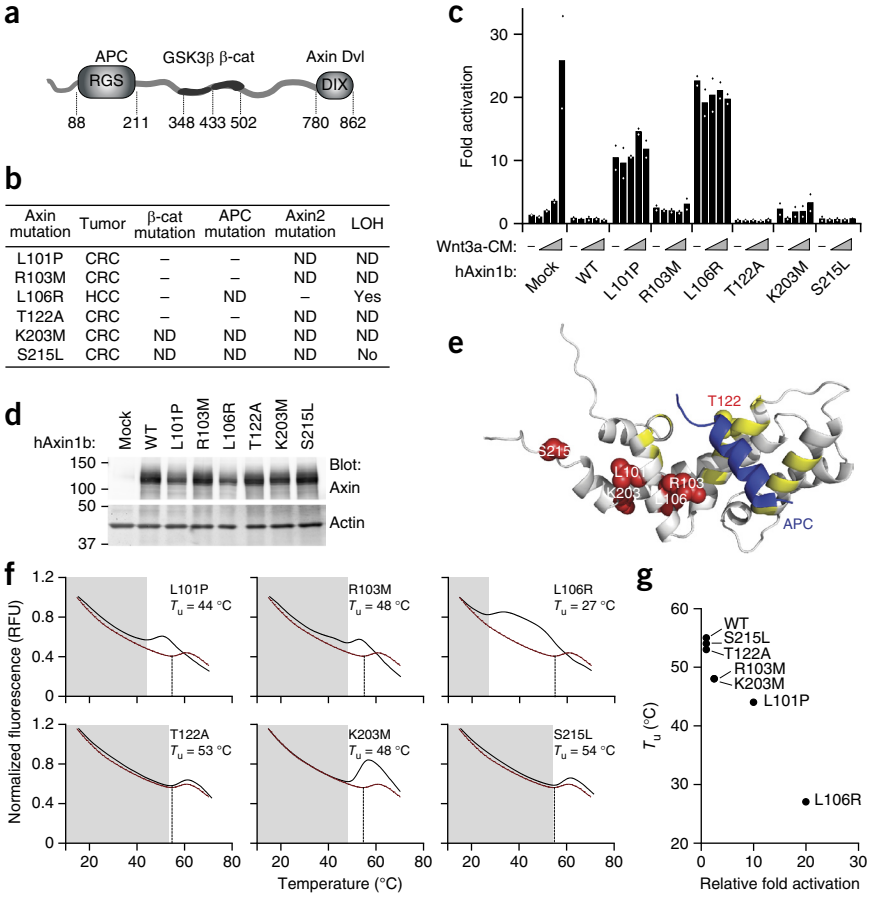

Figure 1 Axin RGS missense mutations induce Wnt-pathway activation and structural destabilization. (**a**) Schematic representation of full-length Axin. GSK3β, glycogen synthase kinase 3 beta; β-cat, β-catenin. (**b**) Axin RGS-domain missense mutants identified in human tumors[20–23]. CRC, colorectal carcinoma; HCC, hepatocellular carcinoma; LOH, loss of heterozygosity; ND, not determined. (**c**) Wnt luciferase-reporter activity in HEK293T cells expressing mock vector, WT Axin or the indicated missense variants, and treated with increasing doses of Wnt3a-conditioned medium (Wnt3a-CM). Graph shows average (bars) and range (diamonds) of luciferase activity in duplicate cell cultures transfected in parallel. One representative experiment of three independent experiments is shown. (**d**) Western blot showing expression of Axin WT and the indicated Axin cancer variants. Molecular weight (kDa) is indicated at left. Actin represents a loading control. Uncropped images of blots are shown in **Supplementary Data Set 1**. (**e**) Structure of human Axin RGS (gray) in complex with APC. Blue, APC SAMP3 peptide; yellow, APC-interacting residues; red space filling, non-APC-binding residues mutated in cancer; yellow space filling, APC-binding T122. From PDB 1EMU and 1DK8 (ref. 18). (**f**) Fluorescence-based thermal denaturation of WT (red dotted lines) and mutant RGS domains (black solid lines) at 340-nm emission. Results represent two independent experiments. Unfolding temperatures (T_u) of WT RGS (55 °C; gray boxes) and mutant Axin variants (vertical dotted lines) are indicated in each graph. RFU, relative fluorescence units. (**g**) Correlation graph of RGS-domain unfolding temperatures and Wnt luciferase-reporter activity observed for individual Axin cancer mutants, as indicated. The calculated Pearson correlation coefficient is r = –0.97, $P = 0.0003$ (two sided; $n = 7$ Axin variants; correlation was calculated with values shown in **c** and **f**).

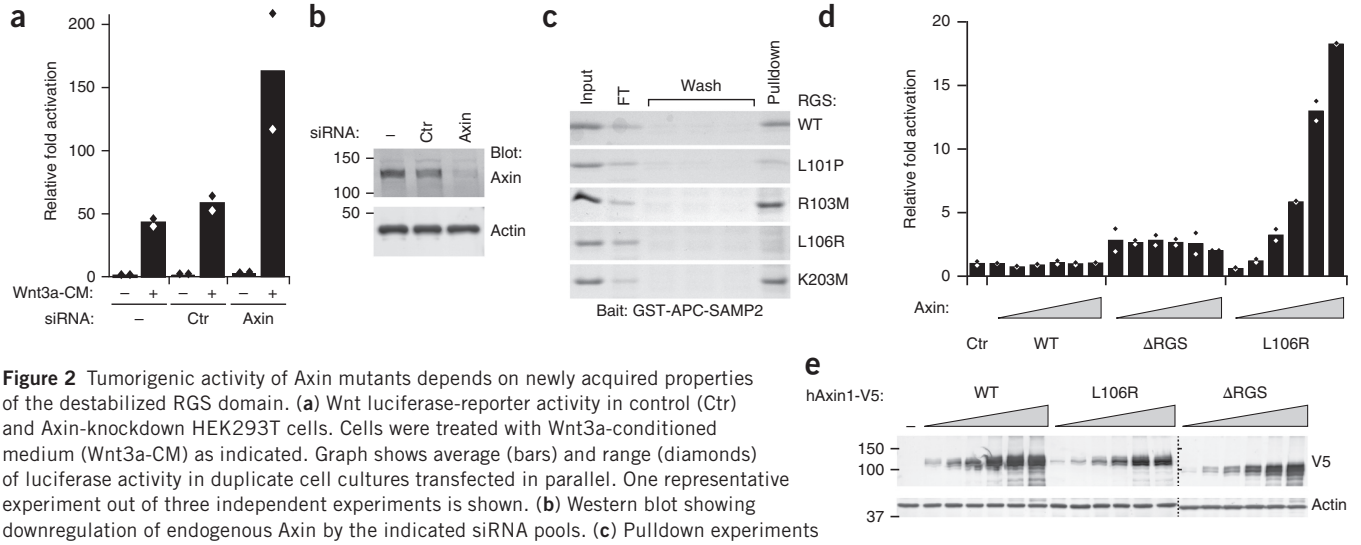

Figure 2 Tumorigenic activity of Axin mutants depends on newly acquired properties of the destabilized RGS domain. (**a**) Wnt luciferase-reporter activity in control (Ctr) and Axin-knockdown HEK293T cells. Cells were treated with Wnt3a-conditioned medium (Wnt3a-CM) as indicated. Graph shows average (bars) and range (diamonds) of luciferase activity in duplicate cell cultures transfected in parallel. One representative experiment out of three independent experiments is shown. (**b**) Western blot showing downregulation of endogenous Axin by the indicated siRNA pools. (**c**) Pulldown experiments in which *Escherichia coli*–purified GST-tagged APC SAMP2 motif (L1660–D1841; GST-APC-SAMP2) was used as a bait to determine direct interactions with WT or mutant purified RGS domains, as indicated. Levels of APC-bound RGS protein are shown in eluate (wash) lanes. Input and flow through (FT) are shown for comparison. The results represent two independent experiments. (**d**) Wnt luciferase-reporter activity in HEK293T cells with increasing expression of the indicated Axin variants (6.25, 12.5, 25, 50, 100 or 200 ng of transfected DNA). Graph shows average (bars) and range (diamonds) of luciferase activity in duplicate cell cultures transfected in parallel. (**e**) Western blot showing protein expression levels of the experiment in **d**. Uncropped images of blots throughout figure are shown in **Supplementary Data Set 1**. Actin represents a loading control.

RGS destabilization endows Axin with tumorigenic properties

We then investigated whether conventional loss of function of Axin might be responsible for the induction of β-catenin–mediated transcription, by using human HEK293T cells. Short interfering RNA (siRNA)-mediated depletion of Axin to 10% of WT levels did not induce substantial basal β-catenin–mediated transcription but instead enhanced cellular responses to Wnt (**Fig. 2a**,**b**), as shown previously[24]. Hence, the mechanism by which Axin RGS mutants drive β-catenin activation in these cells appears to be not merely due to a reduction in the functional pool of Axin.

Binding of RGS L101P and RGS L106R to APC was strongly impaired, consistently with these mutants' loss of structural integrity (**Fig. 2c**). In contrast to the concentration-dependent induction of β-catenin–mediated transcription by the Axin L106R cancer mutant, an RGS-deleted variant of Axin (Axin ΔRGS) failed to induce substantial β-catenin activation over a range of tested protein concentrations (**Fig. 2d**,**e**). Thus, Axin ΔRGS largely retained tumor-suppressor activity, in line with previous reports[25,26]. In conclusion, it is not the loss of RGS function but the acquired destabilization that endows the Axin cancer mutants with new tumorigenic properties.

Unstable RGS forms nanoaggregates with disordered tentacles

To gain molecular insight into the structural defects of the Axin RGS mutants, we analyzed RGS-domain fragments of the most potent cancer variant, L106R, by NMR spectroscopy (**Fig. 3**). We acquired 2D HSQC spectra of ^{15}N-labeled RGS WT (**Fig. 3b**) and RGS L106R mutant proteins (**Fig. 3c** and **Supplementary Fig. 1c**). Such spectra provided a fingerprint of the backbone of the folded protein, thus allowing us to monitor disturbances in the native structure at the level of individual residues. NMR spectra of RGS WT showed a spread signal pattern typical for a folded protein. In spectra of destabilized RGS L106R,

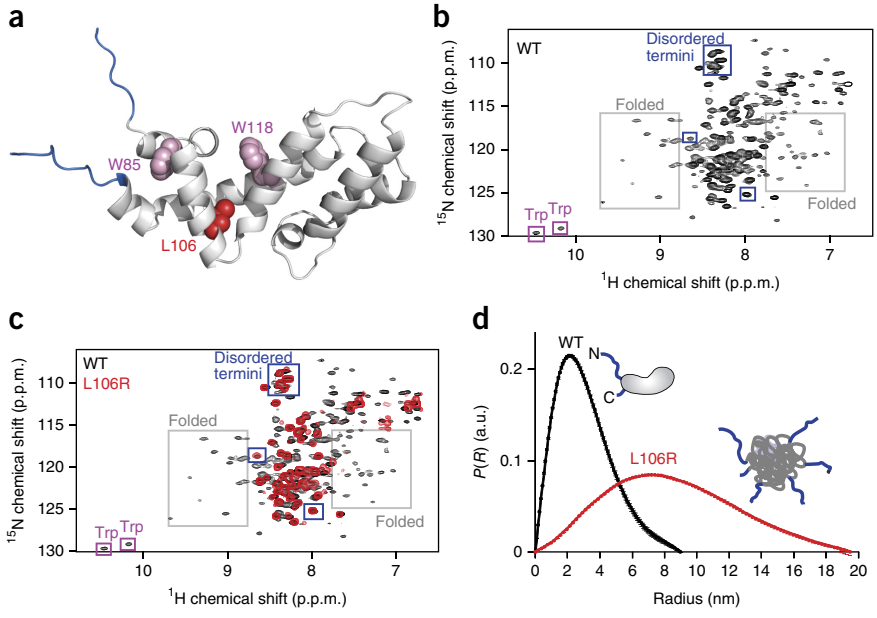

Figure 3 Axin L106R RGS forms oligomers with disordered extensions. (**a**) Structure of the Axin RGS domain. Purple, tryptophan side chains W85 and W118; red space filling, L106. From 1DK8 (ref. 18). (**b**) 2D NMR spectra showing signals of WT RGS (WT). Tryptophan side chain signals (purple squares), signals from folded regions (gray squares) and signals from disordered termini (blue squares) are indicated. (**c**) Overlapping 2D NMR spectra (collected at 25 °C) of WT RGS (WT; black) and RGS L106R (red). (**d**) SAXS data (collected at 25 °C) showing size distribution (radius) of the RGS L106R domain (red) compared to RGS WT (WT; black). Inset models illustrate the loss of RGS structure in the L106R mutant. *P*(*R*), interatomic distance distribution function; a.u., arbitrary units.

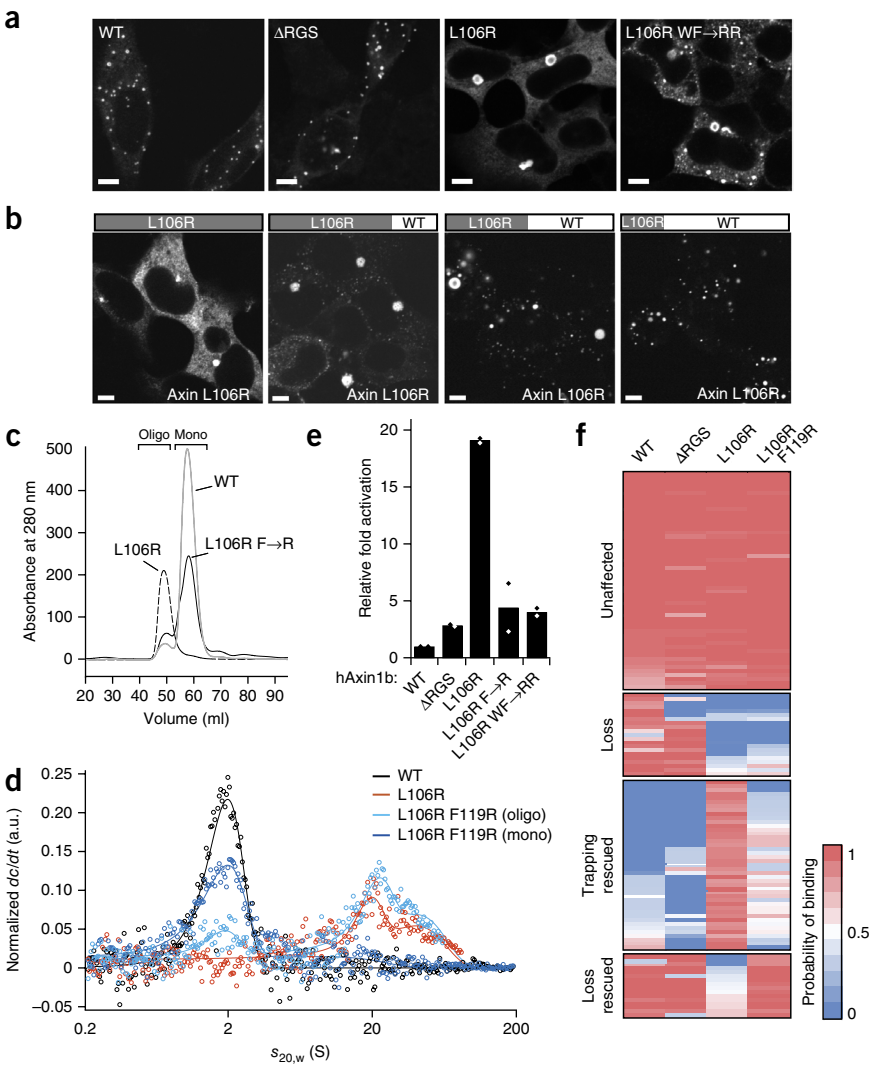

Figure 4 Interference with oligomerization rescues tumor-suppressor activity of Axin L106R. (**a**) Confocal microscopy of WT, ΔRGS, L106R and L106R W118R F119R (L106R WF→RR) Axin variants in HEK293T cells. Scale bars, 10 μm. (**b**) Confocal microscopy of GFP-tagged Axin L106R expressed alone or coexpressed with increasing levels of V5-tagged WT Axin (WT) in a 4:1, 1:1 or 1:4 ratio. Scale bars, 10 μm. (**c**) SEC analysis of purified RGS WT, RGS L106R and RGS L106R F119R (L106R F→R) domains. Monomeric (mono) and oligomeric (oligo) fractions are indicated. The RGS L106R mutant eluted in the soluble void fraction at 50 ml. (**d**) AUC data of RGS WT, RGS L106R and RGS L106R F119R SEC fractions (as shown in **c**). An overlay of the AUC data of RGS WT (black), RGS L106R (red), oligomeric RGS L106R F119R (dark blue) and monomeric RGS L106R F119R (light blue) is shown. Normalized concentration change over time (*dc/dt*) was plotted against standardized sedimentation coefficient ($s_{20,w}$) values. A.u., arbitrary units. Oligomeric species appeared at sedimentation coefficients ranging from 8 up to 100 S, compared to 2 S for the monomeric peak. (**e**) Wnt luciferase gene-reporter activity of Axin WT (WT), Axin ΔRGS, Axin L106R, Axin L106 F119R (L106R *F*→R) and Axin L106R W118R F119R (L106R WF→RR) in HEK293T cells. Graph shows average (bars) and range (diamonds) of luciferase activity in duplicate cell cultures transfected in parallel. (**f**) Analysis of interactomes of Axin WT (WT), Axin ΔRGS, Axin L106R and Axin L106R F119R in HEK293T cells. Flag-tagged Axin variants were expressed in HEK293T cells, and associated proteins were analyzed by MS. Heat map shows the probability of interaction of individual partner proteins with indicated Axin variants. Shown categories represent 25% of all binders.

signals corresponding to the natively disordered N- and C-terminal extensions were still present (N2–Y70 and S215–V220; **Fig. 3c** and **Supplementary Fig. 1c**). However, we observed a dramatic loss of NMR signals corresponding to residues in the folded region of the protein, including the signals of both tryptophan side chains, which were clearly visible in the spectra of the WT at approximately 9 p.p.m. This result is consistent with destruction of the hydrophobic core.

Consequently, we applied small-angle X-ray scattering (SAXS) to analyze whether the unfolded nature might lead to aberrant oligomerization of the mutant protein. SAXS is a solution scattering method that determines shape parameters, such as the maximal extension of a complex (maximum diameter) and the average distance of the atoms from the gravity center of the complex (radius of gyration (R_g)). RGS WT comprised a monomeric globular domain with an average R_g of 2.3 nm and a maximum diameter (D_{max}) of 9 nm (**Fig. 3d**; apparent molecular ratio 26 kDa). In contrast, the dimensions of RGS L106R were clearly enlarged (R_g of 7.2 nm; D_{max} of 19 nm), thus indicating the formation of nanometer-scale aggregates of at least 4 or5 molecules (**Fig. 3d**). Zero-angle intensity ($I(0)$) analysis revealed an apparent molecular ratio of RGS nanoaggregates of 120 kDa over a wide concentration range (20–80 μM). The formation of such nanoaggregates is in agreement with the observed loss of NMR signals in the hydrophobic core, because increased particle size strongly reduces NMR signal intensity, owing to slower tumbling[27]. The disordered N and C termini still remained visible in the NMR spectra, thus indicating that they remained dynamic (**Fig. 3c**). Hence, these termini are not part of the oligomeric core but instead protrude and remain solvent exposed. We conclude that mutation-induced loss of RGS structure leads to the formation of nonamyloid, soluble nanoaggregates that still expose disordered regions of Axin such that they can engage with binding partners.

RGS aggregation interferes with Axin self-polymerization

We next analyzed whether RGS L106R self-association might interfere with Axin-complex assembly in the cell. Overexpressed Axin typically forms highly dynamic cytoplasmic puncta, in a process mediated by polymerization of its C-terminal DIX domain[19,28] (**Figs. 1a** and **4a**). Axin L106R failed to form puncta, displaying a diffuse cytosolic localization. In a subset of cells, the protein partially accumulated in perinuclear structures reminiscent of aggresomes, in which misfolded proteins typically accumulate[29] (**Fig. 4a** and **Supplementary Fig. 2a–c**). These structures formed in a concentration-dependent manner (**Supplementary Fig. 2a**) and localized to the microtubule-organizing center (**Supplementary Fig. 2b**) but did not recruit HDAC6 or vimentin, two commonly used markers for aggresomes[29,30] (**Supplementary Fig. 2c**). Of note, even in cells carrying aggresome-like structures, the majority (76%) of the mutant Axin protein resided in the diffuse cytosolic fraction, as quantified by fluorescence intensity.

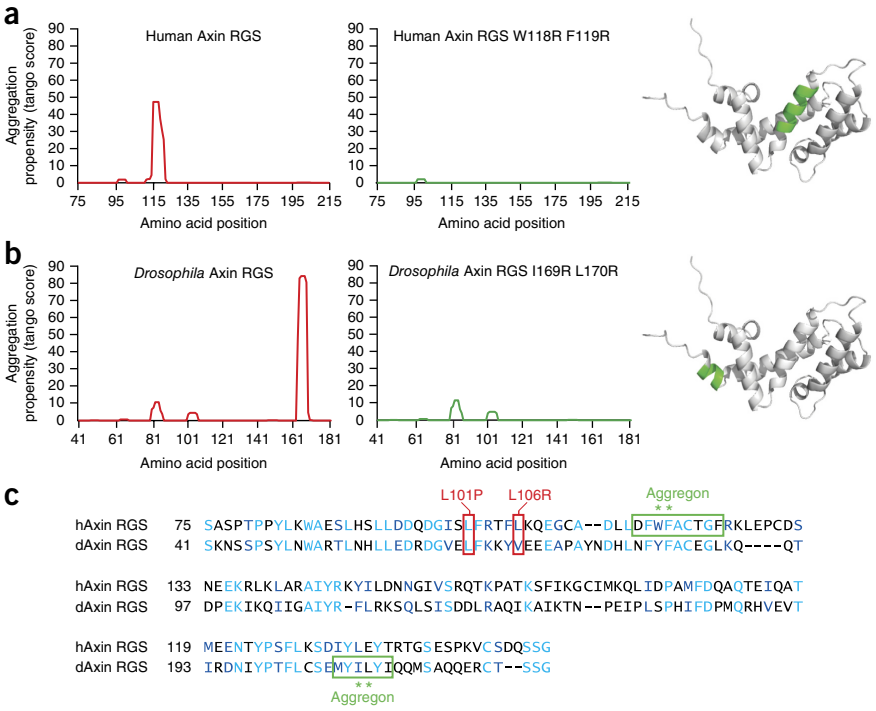

Figure 5 TANGO prediction of aggregation-prone sequences in human and *Drosophila* Axin RGS. (**a**,**b**) Aggregation propensity of Axin RGS predicted by TANGO, before and after amino acid substitutions in aggregons for *Homo sapiens* (**a**) and *Drosophila melanogaster* (**b**). Structures depict the shift in aggregon location for human and *Drosophila* RGS. (**c**) Alignment of *H. sapiens* (h) and *D. melanogaster* (d) Axin RGS-domain amino acid sequences. Mutated residues found in cancer are outlined in red. Aggregons derived from predictions in **a** and **b** are outlined in green. Asterisks indicate mutated aggregon residues. Cyan, conserved; blue, semiconserved; black, nonconserved.

This subcellular localization pattern of Axin L106R was strikingly distinct from that of Axin ΔRGS, which formed puncta indistinguishable from those of Axin WT (**Fig. 4a**). Thus, the conformational conversion of the RGS domain rather than its loss altered the mode of Axin-complex assembly. To characterize the aggregates of mutant Axin in cells, we assessed their SDS solubility. Axin L106R displayed high solubility in SDS-containing buffers, similarly to the WT protein (**Supplementary Fig. 2d**), thus indicating that it does not form amyloid-type aggregates in cells.

After coexpression of increasing amounts of Axin WT, Axin L106R localization shifted from the diffuse cytosolic pool and aggresome-like structures and colocalized with Axin WT in puncta (**Fig. 4b**). These findings suggest that mutation-induced aggregation of the N-terminal RGS domain disables DIX-dependent polymerization of the Axin C terminus. An excess of WT Axin prevents the mutant protein from making aberrant RGS-RGS contacts, thus allowing the mutant protein to be incorporated in Axin WT multimerized complexes, probably through DIX domain–mediated interactions[19]. Concordantly with these observations, increasing doses of Axin WT suppressed the Axin L106R–mediated induction of β-catenin–mediated transcription (**Supplementary Fig. 3**). Importantly, pathway suppression occurred even in conditions in which mutant Axin was in excess over WT and accumulated in aggresomes (**Fig. 4b** and **Supplementary Fig. 3**), thus suggesting that aggresome formation itself is not a dominant cause of pathway activation.

Preventing RGS aggregation restores Axin function *in vitro*

We then asked whether we could revert the gain-of-function phenotype by suppressing Axin aggregation. We used the algorithm TANGO to predict aggregation propensity in the Axin protein sequence[31] (**Fig. 5a**). Strikingly, human Axin RGS carries only one prominent aggregation-prone segment (D116–F124), which is probably responsible for aggregation of this protein. This segment is buried in the WT protein but is potentially accessible in mutants. We therefore introduced additional F119R or W118R F119R mutations in the aggregation-prone segment of Axin L106R. These mutations were unable to restore stability (**Supplementary Fig. 4a**) but were predicted to specifically suppress aggregation (**Fig. 5a**). Remarkably, RGS L106R F119R partially restored monomerization *in vitro*, as shown by size-exclusion chromatography (SEC) and analytical ultracentrifugation (AUC) (**Fig. 4c**,**d**). This result indicates that Axin RGS nanoaggregation is mediated by the segment D116–F124. For clarity, we defined this segment, the aggregon, as an experimentally verified stretch responsible for aggregation. Moreover, full-length Axin L106R F119R or Axin L106R W118R F119R also regained the ability to form cytosolic puncta in cells (**Fig. 4a**) and to prevent excess Wnt signaling (**Fig. 4e** and **Supplementary Fig. 4b–d**). Accordingly, suppression of aggregation by F119R was sufficient to revert the Axin L106R phenotype, despite not restoring the RGS fold (**Supplementary Fig. 4a**). Thus, the nanoaggregates are the actual oncogenic species.

Mutation-induced aggregation rewires the Axin interactome

To gain understanding of why nanoscale aggregation of Axin derails Wnt signaling, we analyzed the interactomes of Axin WT and mutant proteins in human cells (**Fig. 4f** and **Supplementary Table 1**). The destabilizing L106R mutant led to reduced binding of 34 of 115 partners of Axin WT and a gain of 196 new contacts, thus indicating a substantial rewiring of the interactome. However, introduction of the aggregon suppressor mutation considerably restored the Axin interactome (16 partners reconnected and 43 trapped partners released; **Fig. 4f**).

STRING[32] analysis of Axin-interacting proteins that co-regulate cellular processes confirmed that Axin WT is central to the formation of a protein network involved in the regulation of β-catenin turnover and interacts with a regulatory phosphatase complex (**Supplementary Fig. 5a**). Comparison of interactomes revealed that a number of known Wnt-pathway components (GSK3β, CK1, β-catenin, Dvl2 and Dvl3) remained bound to all Axin variants, whereas others progressively lost binding to Axin ΔRGS (APC and FAM123B) and Axin L106R (APC, FAM123B, TNKS and TNKS2) (**Supplementary Fig. 5b**,**c**). Moreover, a third cluster of Axin-binding proteins comprised the eight subunits of the Gid complex, a large highly conserved E3 ubiquitin ligase complex involved in the regulation of gluconeogenesis in yeast[33,34]. Of note, interaction with Gid-complex subunits was selectively lost for Axin L106R, whereas the aggregon suppressor mutation restored binding (**Supplementary Fig. 5c**,**d**), thus revealing a potential role for altered regulation of glucose metabolism by Axin cancer mutants.

Our analysis predicted the large number of newly identified interactions of the Axin L106R cancer mutant to function in a diverse set

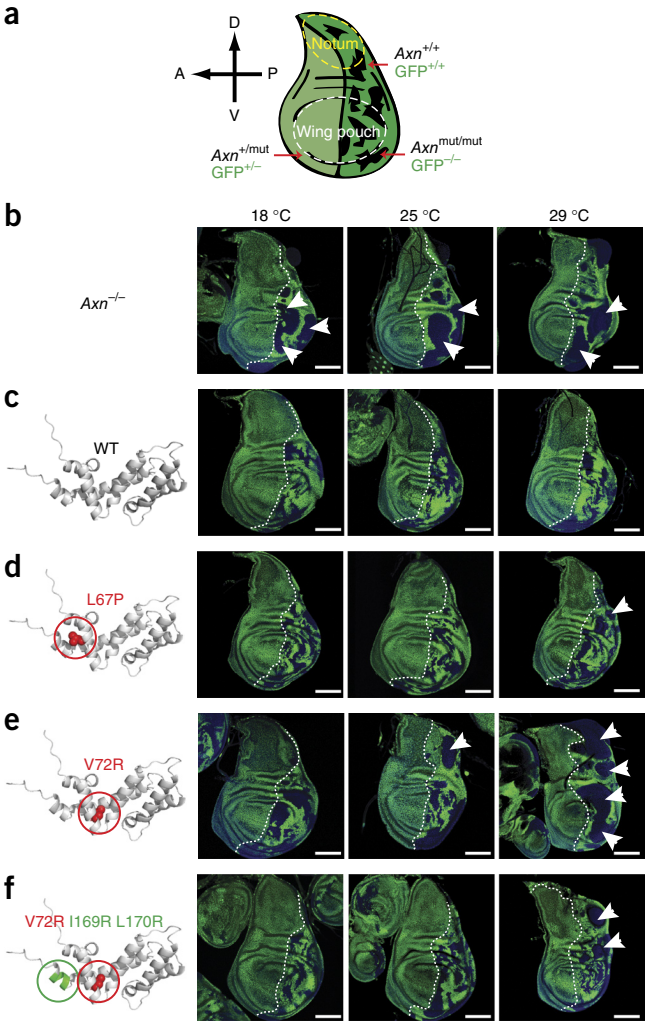

Figure 6 *In vivo* temperature-dependent hyperplastic growth induced by *Drosophila* Axin cancer mutants is rescued by aggregon mutations. (**a**) Schematic representation of late third-instar *Drosophila* wing imaginal disc, illustrating the experimental setup. The central pouch, which will form the adult wing proper, and the surrounding tissues, which will develop into the hinge and part of the thorax (the notum), are indicated. cDNAs encoding WT and mutant Axin were integrated at the endogenous *Axn* locus in the posterior compartment (black patches). The anterior compartment illustrates the phenotype of the heterozygous mutant $Axn^{+/mut}$. A, anterior; P, posterior; D, dorsal; V, ventral. (**b**–**f**) Mosaic wing imaginal discs from larvae expressing the indicated dAxin variants and grown at 18 °C, 25 °C or 29 °C. Absence of GFP marks cells made homozygous for the indicated mutation. White arrows indicate tumor-like growth. Scale bars, 100 µm. (**b**) Clonal deletion of *Axn* (GFP-negative cells) in *Drosophila* wing discs. Growth temperatures are indicated. White arrows indicate tumor-like growth. (**c**) dAxin WT clones (GFP-negative cells) in *Drosophila* wing discs. (**d**) dAxin L67P clones (GFP-negative cells) in *Drosophila* wing discs. White arrow indicates partial tumor-like growth at 29 °C. (**e**) dAxin V72R clones (GFP-negative cells) in *Drosophila* wing discs. White arrows indicate tumor-like growth at 25 °C and 29 °C. (**f**) Introduction of I169R L170R aggregon mutations in dAxin V72R clones. White arrows indicate partial tumor-like growth at 29 °C.

of cellular processes, including mitosis, DNA-damage repair, protein trafficking and protein turnover (**Supplementary Fig. 5e**). A protein cluster comprising seven components of the 26S proteasome was found to selectively bind the aggregation-prone Axin L106R mutant but not to interact with the Axin L106R F119R aggregon suppressor mutant (**Supplementary Fig. 5e**). Thus, trapping of these proteasomal subunits by Axin L106R requires the aggregated state of Axin.

We conclude that the Axin interactome is substantially rewired by mutation-induced nanoaggregation, whereas loss of the RGS domain displays relatively mild effects. Thus, selective aggregation-dependent alterations in the Axin network are a likely cause of aberrant Wnt-signaling activation and a potential growth advantage driven by destabilizing Axin mutations.

Axin RGS cancer mutants induce tumor-like growth *in vivo*

To assess the *in vivo* relevance of Axin aggregates, we used *Drosophila*. *Drosophila* wing imaginal discs provide an established model system to study the physiological activity of various tumor-suppressor genes. Moreover, *Drosophila* Wnt-cascade components show a high degree of conservation with the human system (30% identity and 67% similarity for Axin RGS) (**Fig. 5c**). We used a recently established protocol for homologous recombination[35] to delete the first three exons of the Axin gene and to replace this region with a cassette including an *attP* recombination site (**Supplementary Fig. 6a**,**b**). We then knocked in cDNAs expressing *Drosophila* Axin (dAxin) cancer variants in the endogenous *Axn* locus (**Figs. 5c** and **6a**). As shown previously, clonal deletion of endogenous *Axn* in the posterior compartment of wing imaginal discs overgrew at the expense of surrounding WT tissue[36] (**Fig. 6b** and **Supplementary Fig. 6c**). This phenotype resembles tissue colonization by precancerous cells. Deletion clones exhibited a round shape and a smooth edge (**Fig. 6b**). When we knocked in WT *Axn* in the endogenous locus, mutant clones reverted to their normal jagged and elongated shape and no longer overgrew, as expected (**Fig. 6c** and **Supplementary Fig. 6c**).

Next, we generated clones expressing dAxin V72R, the equivalent of human Axin L106R (**Fig. 5c**). At the standard temperature of 25 °C, these clones appeared normal in the pouch but had aberrantly smooth edges in the prospective notum and hinge (**Fig. 6e**), thus indicating partial loss of function. Because Axin RGS L106R is thermolabile, we analyzed clone behavior at various temperatures. At 29 °C, dAxin V72R clones overgrew at the expense of surrounding WT tissue and displayed smooth edges in all regions (**Fig. 6e** and **Supplementary Fig. 6c**). Moreover, we detected ectopic expression of *senseless* (official symbol *sens*) and *Distal-less* (*Dll*) in dAxin V72R clones, which indicated excess Wingless signaling activity (**Supplementary Fig. 6d**). Of note, heterozygous tissue in the anterior compartment developed normally at all temperatures tested. Lowering the temperature to 18 °C substantially restored dAxin V72R's ability to prevent ectopic signaling (28%; n = 25 independent wing discs) (**Fig. 6e**). dAxin L67P, similarly to moderately destabilized Axin L101P, was also temperature sensitive. This mutant fully rescued the loss of endogenous Axin at 25 °C but showed increased functional impairment at 29 °C (**Fig. 6d**), consistently with our biophysical findings with the human homologs. We conclude that RGS destabilization induces tumor-like growth *in vivo*.

Suppressing aggregation restores mutant Axin function *in vivo*

As a stringent test of the hypothesis that blocking nanoaggregation rescues the activity of destabilizing RGS point mutants, we knocked in Axin RGS aggregon suppressor mutants at the endogenous locus. TANGO predicted only one clear aggregation-prone segment in dAxin (M167–I172), at a strikingly different location from that in human Axin (**Fig. 5a**,**b**). We introduced antiaggregation mutations I169R L170R in this segment of dAxin V72R (**Fig. 5b**). This exchange was sufficient to substantially restore Axin activity in wing discs *in vivo* (**Fig. 6f** and **Supplementary Fig. 6d**). Moreover, whereas

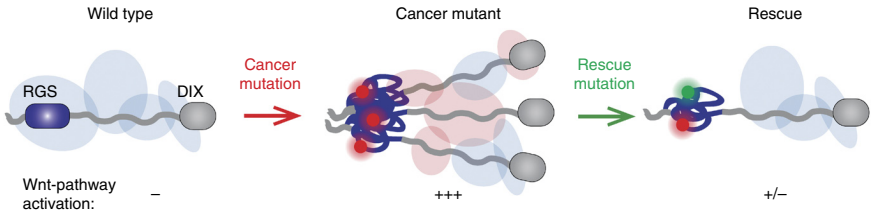

Figure 7 Model for the mechanism of action of Axin RGS cancer variants. Axin WT forms a complex with partner proteins (blue ovals) and mediates tumor-suppressor activity. A single cancer point mutation endows Axin with new properties through formation of an oligomeric core with disordered tentacles. The altered conformation perturbs the associated subproteome (blue and red ovals) through both loss and gain of binding partners. The combined events drive Wnt-pathway activation and tumor growth. Tumorigenic behavior of the mutant protein is corrected by interference with aggregon-mediated oligomer formation.

homozygous V72R mutant flies died at early developmental stages at all temperatures tested, the viability of homozygous V72R I169R L170R mutants was rescued up to the adult stage when flies were grown at 18 °C. Introduction of homologous mutations to the human aggregon suppressor mutant (Y86R F87R) did not restore activity (**Supplementary Fig. 6e**). In line with these findings, the *Drosophila* but not the human aggregon suppressor mutation restored the ability of dAxin V72R to form cytosolic puncta in cells (**Supplementary Fig. 7**). Together, our findings demonstrate that it is not protein instability itself but subsequent protein nanoaggregation that causes tumor-like growth *in vivo*.

DISCUSSION

This study provides a molecular explanation of how cancer-associated missense mutations in the scaffold Axin lead to excess Wnt signaling. Our findings suggest that a subset of Axin point mutants drive tumorigenesis through a mechanism that is not merely caused by the loss of functional Axin. Instead, a single point mutation causes Axin to form soluble nanoaggregates that have tumorigenic activity *in vivo*. These oligomeric species lack typical characteristics of amyloids, such as fibrillar growth *in vitro* and SDS insolubility *in vivo*. Soluble oligomers are seen as major toxic agents in aggregation diseases, as described for Tau, α-synuclein and IAPP, by driving cellular degeneration and neuronal atrophy through a largely elusive mechanism[37,38]. In contrast, nanoaggregates of Axin are associated with tumorigenic growth *in vivo*. A comprehensive understanding of how their molecular mode of action causes a distinct phenotype is key to gaining a picture of the pathogenic mechanism of protein aggregation in general.

We propose the following model based on our findings (**Fig. 7**): Axin WT organizes the formation of a multiprotein complex by recruiting and directing the activity of partner proteins to suppress β-catenin–mediated transcription. In cancer cells, a single destabilizing point mutation endows the Axin protein with new properties, facilitating formation of an oligomeric core with disordered tentacles. The conformational conversion of Axin perturbs the associated interactome, thus resulting in both loss and gain of binding partners. When the mutant protein is in excess, the combined molecular events together trigger β-catenin signaling and drive tumorigenesis. Importantly, tumorigenic behavior of the mutant protein can be corrected by countering aggregation.

How do the aggregation properties of mutant Axin affect signaling? A multitude of proteins interact with Axin, clustering into three functionally distinct complexes[3] (**Supplementary Fig. 5a**). A number of known partners operate together with Axin within the destruction complex, thereby regulating β-catenin turnover. Within this complex, proper timing and positioning of protein interactions is essential to coordinate and direct kinase activity and to allow for the capture and release of the β-catenin substrate protein for subsequent cycles of phosphorylation. In the case of the cancer mutant, nanoaggregation may aberrantly increase the spatial neighborhood of regulatory proteins that bind to the disordered tentacles of Axin. Consequently, the affinity of binding partners would be increased for entropic reasons, but undesired interactions between Axin binding partners might also be triggered. Together with the observed loss of binding of a number of Wnt-pathway regulators, these altered interactions may compromise the molecular activity of the destruction complex and aggravate the tumorigenic phenotype.

The Axin cancer-mutant interactome acquired a large number of new interactions (**Supplementary Fig. 5e**). Gained partners were associated with the regulation of diverse cellular processes, including mitosis, DNA repair, protein trafficking and protein turnover. A fraction of these proteins may represent functional interaction partners that normally interact transiently with the disordered regions of Axin WT but are trapped by the tentacles of the aggregated conformation of the cancer mutant. Other gained partners may represent members of the proteostasis network that recognize misfolded or aggregated proteins. One example is the DNAJB6 protein, which binds only the aggregation-prone Axin mutant and has previously been described to interfere with the formation of larger polyglutamine peptide aggregates[39]. Another notable cluster of proteins that bind the cancer mutant comprises seven subunits of the 26S proteasome. Further insight into how the aggregated form but not the unfolded suppressor mutant of the protein is recognized and processed by the cellular proteostasis network is required to understand how the cancer mutant acquires a sufficient lifetime to perform its tumorigenic activity in the cell.

Aggregation is a conserved consequence of destabilizing mutations in both human and *Drosophila* Axin. Stability-sensitive regions are conserved between species. Unexpectedly, however, neither the sequence nor the location of the aggregon is conserved (**Fig. 5**). Our work thus reveals that the positions of aggregons are not essential for the maintenance of protein folds and activity, and this phenomenon may constitute a general evolutionary principle.

The relevance of destabilizing point mutants has also been shown in other tumor suppressors, particularly for the DNA-binding domain of p53 (ref. 40). *In vivo*, these mutants behave as dominant negatives, and some mutants gain new functions[41]. The mutants can induce large, amorphous aggregates that coaggregate WT p53 and its paralogs p63 and p73, thereby destroying their vital interaction with DNA and preventing their transcriptional activity[42]. Our findings suggest a different mode of action for Axin cancer mutants. First, the Axin mutant oligomers are small and soluble, and they comprise only a few molecules. Second, loss of function of the destabilized mutant domain is not responsible for the tumorigenic behavior of the Axin mutants. Third, Axin mutants do not operate as dominant-negative proteins, as shown by the normal development of heterozygous tissue *in vivo* and the normalization of assembly of mutant Axin complexes by Axin WT coexpression.

From our findings, we conclude that the nanoaggregational conformation of Axin cancer mutants mediates loss of binding and aberrantly

brings in critical binding partners while failing to properly coordinate their activity. The widespread effect of the mutant signaling hub thus derails the signaling circuitry in the cell, potentially affecting cellular processes such as cell division and energy metabolism. Given the overall similarity between the structural features of Axin and those of other tumor suppressors such as BRCA1 and APC, in which folded domains act in concert with large disordered segments, we propose that previously described cancer point mutations may operate through similar mechanisms[43,44]. In this view, cancer mutants that destabilize scaffolds in cancer cells may deregulate multiple pathways by forming nanoaggregates that rewire signaling interactomes.

We demonstrated that for reversion of the oncogenic gain-of-function phenotype it is sufficient to target the aggregon to prevent aggregation. It is not necessary to restore the damaged protein fold, which would be a much more complex goal. This finding opens up new avenues for cancer treatment by small molecules that address the problem of aggregation of the damaged scaffold.

METHODS

Methods and any associated references are available in the online version of the paper.

Accession codes. The MS data have been deposited in the ProteomeXchange Consortium via the Proteomics Identifications (PRIDE) partner repository, under accession code PXD003116.

Note: Any Supplementary Information and Source Data files are available in the online version of the paper.

ACKNOWLEDGMENTS

We thank members of the laboratories of M.M.M. and S.G.D.R. for experimental support, helpful discussions and suggestions. We thank B. Kleizen and I. Braakman (Cellular Protein Chemistry, Bijvoet Centre for Biomolecular Research, Utrecht University) for providing the CFTR ΔF508 construct and H. Bellen (Baylor College of Medicine), I. Duncan and D. Duncan (Washington University) for antibodies. This work was supported by the European Research Council ((ERC) starting grant 242958 to M.M.M. and ERC advanced grant 294523 to J.-P.V.); Utrecht University (High Potential Grants to M.M.M. and S.G.D.R.); Boehringer Ingelheim Fonds (PhD fellowship to E.C.v.K.); the European Union (Framework Programme (FP) 7 Marie Curie ITN 608180 'WntsApp' to M.M.M. and S.G.D.R., FP7 Marie Curie ITN-IDP 317371 'ManiFold' to S.G.D.R., FP6 Marie Curie Excellence Grant 25651 'chaperoning cascades' to S.G.D.R. and BioNMR project 261863 to R.B. and T.M.); the Netherlands Organization for Scientific Research ((NWO) VICI grant to M.M.M., Vidi career development grant to S.G.D.R. and instrumentation support for a TCI probe to R.B.); the Internationale Stichting Alzheimer Onderzoek ((ISAO) grant to S.G.D.R.); the Medical Research Council of Great Britain (grant U117584268 to J.P.V.); the European Molecular Biology Organization ((EMBO) ALTF 983-2009 to H.N.); the Uehara and Kanae Foundations (to H.N.); the Austrian Academy of Sciences (APART-fellowship to T.M.); the Bavarian Ministry of Sciences, Research and the Arts in the framework of the Bavarian Molecular Biosystems Research Network (to T.M.); and the German Research Foundation (Emmy Noether program MA 5703/1-1 to T.M.). T.Y.L. and A.J.R.H. were supported by the NWO embedded roadmap program Proteins@Work (project 184.032.201) and PRIME-XS, grant number 262067, funded by the European Union FP7. We thank the Deutsches Elektronen Synchrotron (DESY) synchrotron radiation facilities for support of the SAXS data collection and B. Demeler for providing a license for the UltraScan software package.

AUTHOR CONTRIBUTIONS

Z.A., H.N., E.C.v.K., J.-P.V., S.G.D.R. and M.M.M. conceived and designed the experiments. Z.A., H.N., E.C.v.K., T.B., M.S., I.J., M.V., T.Y.L., R.C.v.S., I.K. and K.R. performed the experiments. Z.A., H.N., E.C.v.K., I.J., T.Y.L., M.V., T.M., R.B., A.J.R.H., J.-P.V., S.G.D.R. and M.M.M. analyzed the data. Z.A., J.-P.V., E.C.v.K., S.G.D.R. and M.M.M. wrote the manuscript. The other authors commented on the manuscript.

COMPETING FINANCIAL INTERESTS

The authors declare no competing financial interests.

1. Good, M.C., Zalatan, J.G. & Lim, W.A. Scaffold proteins: hubs for controlling the flow of cellular information. *Science* **332**, 680–686 (2011).
2. Cortese, M.S., Uversky, V.N. & Dunker, A.K. Intrinsic disorder in scaffold proteins: getting more from less. *Prog. Biophys. Mol. Biol.* **98**, 85–106 (2008).
3. Luo, W. & Lin, S.C. Axin: a master scaffold for multiple signaling pathways. *Neurosignals* **13**, 99–113 (2004).
4. Noutsou, M. *et al.* Critical scaffolding regions of the tumor suppressor Axin1 are natively unfolded. *J. Mol. Biol.* **405**, 773–786 (2011).
5. Mark, W.Y. *et al.* Characterization of segments from the central region of BRCA1: an intrinsically disordered scaffold for multiple protein-protein and protein-DNA interactions? *J. Mol. Biol.* **345**, 275–287 (2005).
6. Minde, D.P., Anvarian, Z., Rüdiger, S.G.D. & Maurice, M.M. Messing up disorder: how do missense mutations in the tumor suppressor protein APC lead to cancer? *Mol. Cancer* **10**, 101 (2011).
7. Szabo, C.I., Worley, T. & Monteiro, A.N. Understanding germ-line mutations in BRCA1. *Cancer Biol. Ther.* **3**, 515–520 (2004).
8. Salahshor, S. & Woodgett, J.R. The links between axin and carcinogenesis. *J. Clin. Pathol.* **58**, 225–236 (2005).
9. Polakis, P. The many ways of Wnt in cancer. *Curr. Opin. Genet. Dev.* **17**, 45–51 (2007).
10. Hart, M.J., de los Santos, R., Albert, I.N., Rubinfeld, B. & Polakis, P. Downregulation of beta-catenin by human Axin and its association with the APC tumor suppressor, beta-catenin and GSK3 beta. *Curr. Biol.* **8**, 573–581 (1998).
11. Ikeda, S. *et al.* Axin, a negative regulator of the Wnt signaling pathway, forms a complex with GSK-3beta and beta-catenin and promotes GSK-3beta-dependent phosphorylation of beta-catenin. *EMBO J.* **17**, 1371–1384 (1998).
12. Itoh, K., Krupnik, V.E. & Sokol, S.Y. Axis determination in *Xenopus* involves biochemical interactions of axin, glycogen synthase kinase 3 and beta-catenin. *Curr. Biol.* **8**, 591–594 (1998).
13. Sakanaka, C., Weiss, J.B. & Williams, L.T. Bridging of beta-catenin and glycogen synthase kinase-3beta by axin and inhibition of beta-catenin-mediated transcription. *Proc. Natl. Acad. Sci. USA* **95**, 3020–3023 (1998).
14. Clevers, H. & Nusse, R. Wnt/β-catenin signaling and disease. *Cell* **149**, 1192–1205 (2012).
15. MacDonald, B.T., Tamai, K. & He, X. Wnt/beta-catenin signaling: components, mechanisms, and diseases. *Dev. Cell* **17**, 9–26 (2009).
16. Reya, T. & Clevers, H. Wnt signalling in stem cells and cancer. *Nature* **434**, 843–850 (2005).
17. Dow, L.E. *et al.* Apc restoration promotes cellular differentiation and reestablishes crypt homeostasis in colorectal cancer. *Cell* **161**, 1539–1552 (2015).
18. Spink, K.E., Polakis, P. & Weis, W.I. Structural basis of the Axin-adenomatous polyposis coli interaction. *EMBO J.* **19**, 2270–2279 (2000).
19. Schwarz-Romond, T. *et al.* The DIX domain of Dishevelled confers Wnt signaling by dynamic polymerization. *Nat. Struct. Mol. Biol.* **14**, 484–492 (2007).
20. Taniguchi, K. *et al.* Mutational spectrum of beta-catenin, AXIN1, and AXIN2 in hepatocellular carcinomas and hepatoblastomas. *Oncogene* **21**, 4863–4871 (2002).
21. Webster, M.T. *et al.* Sequence variants of the axin gene in breast, colon, and other cancers: an analysis of mutations that interfere with GSK3 binding. *Genes Chromosom. Cancer* **28**, 443–453 (2000).
22. Shimizu, Y. *et al.* Frequent alterations in the Wnt signaling pathway in colorectal cancer with microsatellite instability. *Genes Chromosom. Cancer* **33**, 73–81 (2002).
23. Jin, L.H. *et al.* Detection of point mutations of the Axin1 gene in colorectal cancers. *Int. J. Cancer* **107**, 696–699 (2003).
24. Major, M.B. *et al.* Wilms tumor suppressor WTX negatively regulates WNT/beta-catenin signaling. *Science* **316**, 1043–1046 (2007).
25. Peterson-Nedry, W. *et al.* Unexpectedly robust assembly of the Axin destruction complex regulates Wnt/Wg signaling in *Drosophila* as revealed by analysis *in vivo*. *Dev. Biol.* **320**, 226–241 (2008).
26. Oosterveen, T. *et al.* Two functionally distinct Axin-like proteins regulate canonical Wnt signaling in *C. elegans*. *Dev. Biol.* **308**, 438–448 (2007).
27. Wüthrich, K. NMR studies of structure and function of biological macromolecules (Nobel Lecture). *J. Biomol. NMR* **27**, 13–39 (2003).
28. Schwarz-Romond, T., Merrifield, C., Nichols, B.J. & Bienz, M. The Wnt signalling effector Dishevelled forms dynamic protein assemblies rather than stable associations with cytoplasmic vesicles. *J. Cell Sci.* **118**, 5269–5277 (2005).
29. Johnston, J.A., Ward, C.L. & Kopito, R.R. Aggresomes: a cellular response to misfolded proteins. *J. Cell Biol.* **143**, 1883–1898 (1998).
30. Kawaguchi, Y. *et al.* The deacetylase HDAC6 regulates aggresome formation and cell viability in response to misfolded protein stress. *Cell* **115**, 727–738 (2003).
31. Fernandez-Escamilla, A.M., Rousseau, F., Schymkowitz, J. & Serrano, L. Prediction of sequence-dependent and mutational effects on the aggregation of peptides and proteins. *Nat. Biotechnol.* **22**, 1302–1306 (2004).
32. Jensen, L.J. *et al.* STRING 8: a global view on proteins and their functional interactions in 630 organisms. *Nucleic Acids Res.* **37**, D412–D416 (2009).
33. Menssen, R. *et al.* Exploring the topology of the Gid complex, the E3 ubiquitin ligase involved in catabolite-induced degradation of gluconeogenic enzymes. *J. Biol. Chem.* **287**, 25602–25614 (2012).

34. Francis, O., Han, F. & Adams, J.C. Molecular phylogeny of a RING E3 ubiquitin ligase, conserved in eukaryotic cells and dominated by homologous components, the muskelin/RanBPM/CTLH complex. *PLoS One* **8**, e75217 (2013).
35. Baena-Lopez, L.A., Alexandre, C., Mitchell, A., Pasakarnis, L. & Vincent, J.P. Accelerated homologous recombination and subsequent genome modification in *Drosophila*. *Development* **140**, 4818–4825 (2013).
36. Vincent, J.P., Kolahgar, G., Gagliardi, M. & Piddini, E. Steep differences in wingless signaling trigger Myc-independent competitive cell interactions. *Dev. Cell* **21**, 366–374 (2011).
37. Eisenberg, D. & Jucker, M. The amyloid state of proteins in human diseases. *Cell* **148**, 1188–1203 (2012).
38. Chiti, F. & Dobson, C.M. Protein misfolding, functional amyloid, and human disease. *Annu. Rev. Biochem.* **75**, 333–366 (2006).
39. Gillis, J. *et al.* The DNAJB6 and DNAJB8 protein chaperones prevent intracellular aggregation of polyglutamine peptides. *J. Biol. Chem.* **288**, 17225–17237 (2013).
40. Bullock, A.N. & Fersht, A.R. Rescuing the function of mutant p53. *Nat. Rev. Cancer* **1**, 68–76 (2001).
41. Freed-Pastor, W.A. & Prives, C. Mutant p53: one name, many proteins. *Genes Dev.* **26**, 1268–1286 (2012).
42. Xu, J. *et al.* Gain of function of mutant p53 by coaggregation with multiple tumor suppressors. *Nat. Chem. Biol.* **7**, 285–295 (2011).
43. Rowling, P.J., Cook, R. & Itzhaki, L.S. Toward classification of BRCA1 missense variants using a biophysical approach. *J. Biol. Chem.* **285**, 20080–20087 (2010).
44. Stehr, H. *et al.* The structural impact of cancer-associated missense mutations in oncogenes and tumor suppressors. *Mol. Cancer* **10**, 54 (2011).

ONLINE METHODS

Cell culture. Human embryonic kidney (HEK)293T cells (ATCC CRL-3216) were cultured in RPMI GlutaMAX (Invitrogen) supplemented with 10% FBS (GE Healthcare) and 100 units/mL penicillin and 100 µg/mL streptomycin (Invitrogen), at 37 °C in 5% CO_2. Wnt3a-conditioned medium (Wnt3a-CM) was obtained from mouse L cells (ATCC CRL-2648) stably expressing and secreting Wnt3a, as described previously[45]. Mycoplasma-free status was confirmed routinely every 3 months. Cell lines were not recently authenticated.

Plasmids. Human Axin1 isoform b (NM_181050; IMAGE ID 5809104) with C-terminal V5 or 2×Flag tags was subcloned into pcDNA4T/O (Invitrogen) by standard PCR methods. GFP-tagged human Axin1b was subcloned into pcDNA3.1(+). For bacterial expression, human Axin RGS (N2-V220) was cloned into pET50b(+) (Novagen), and a TEV-cleavage site was added to the RGS N terminus. Mutations introduced by site-directed mutagenesis (Stratagene) were verified by sequencing. For Axin ΔRGS, residues G74 to V220 were deleted. GST-tagged APC SAMP2 (L1660–D1841) was generated by subcloning into pGEX-4T-3 (GE Healthcare).

Luciferase reporter assay. Luciferase TOPflash and FOPflash reporter assays were performed as previously described[46]. 100 ng of Axin-encoding plasmid DNA was transfected in a single well of a 24-well plate (total transfected DNA 250 ng), unless otherwise indicated. Transfection efficiency was controlled and normalized by including a constant amount of TK-*Renilla* reporter plasmid in all transfections. Wnt3a-conditioned medium was added 16 h before cells were harvested. siRNA-induced Axin knockdown was performed by transfection of 5 pmol Axin siRNA (Ambion) with Lipofectamine2000 (Invitrogen). Cells were lysed in passive lysis buffer (Promega), and luciferase activities were measured with the dual luciferase reporter assay system (Promega) according to the manufacturer's instructions.

Protein purification. Axin RGS proteins were expressed as HisNusA fusion proteins in *E. coli* Rosetta cells. Protein expression was induced in 1-l bacterial cultures (OD_{600} of 0.8) with 0.5 mM IPTG at 18 °C for 20 h. Bacterial pellets were resuspended in 50 mM Tris, pH 7.4, 300 mM NaCl, 20 mM imidazole, 5 mM β-mercaptoethanol and cocktail A (1 mM PMSF, Complete Protease Inhibitor Cocktail (Roche), 20 mg/L lysozyme, 10 mg/L DNase and 10 mg/L RNase) and were subsequently lysed by sonication. Lysates were cleared by centrifugation for 30 min at 4 °C (12,000 r.p.m.; Eppendorf 5415R) and filtration (0.45 µm). Proteins were purified on an ÄKTA Purifier system (GE Healthcare) with HisTrap HP columns (GE Healthcare) and exchanged into 50 mM Tris, pH 7.4, and 150 mM NaCl buffer with HiTrap Desalting columns (GE Healthcare). After addition of 1 mM PMSF and 1 mM DTT, the HisNusA tag was cleaved by recombinant His-tagged TEV protease (as described in refs. 4,47). Next, RGS proteins were purified to >95% by removal of the His-NusA and His-TEV tags on a HisTrap HP column. For purification of ^{15}N-labeled RGS proteins, bacteria were grown in M9 minimal medium enriched with $^{15}NH_4Cl$ (Cambridge Isotope Laboratories).

For SEC, AUC, SAXS, and NMR measurements, the Axin RGS proteins were also expressed as HisProteinA fusion constructs in *E. coli* BL-21 cells. After 1 l of bacterial culture had reached an OD_{600} of 0.8 at 37 °C, expression was induced with 0.5 mM IPTG for 20 h at 19 °C. Cells were harvested, and lysis was performed by sonication in 50 mM sodium phosphate buffer, pH 8, 1 M NaCl, 5 mM imidazole, 5 mM β-mercaptoethanol and Serva Protease Inhibitor Cocktail HP (Serva Electrophoresis). Debris was pelleted by centrifugation (4 °C, 15,000 r.c.f., 30 min) and lysates were subsequently filtered through cellulose acetate membranes (0.45-µm and 0.22-µm pore size). Immobilized metal affinity chromatography was performed with a 5-ml HisTrap HP column on an ÄKTA Purifier system (GE Healthcare) with 50 mM sodium phosphate buffer, pH 8, 1 M NaCl, and 5 mM β-mercaptoethanol) containing 5 mM imidazole (buffer A) or 1 M imidazole (buffer B) for gradient formation. After the column was loaded, it was washed with buffer A until a stable baseline was reached under UV at 280 nm. Next, the column was washed with 5% B and eluted with 25% B, and 5 ml of the collected peak was applied to a size-exclusion column (HiLoad Sepharose 16/600 pg75, GE Healthcare) on an ÄKTA Pure system (GE Healthcare) at RT. The corresponding running buffer was composed of 50 mM Tris, pH 8, 500 mM NaCl and 2 mM β-mercaptoethanol.

GST-SAMP2 protein expression was induced at 30 °C for 6 h. Bacterial pellets were resuspended in PBS with 1% BSA, 1 mM DTT, 1 mM EDTA and protease-inhibitor cocktail and lysed as described above. Lysates were incubated for 1 h with glutathione Sepharose beads (GE Healthcare). Beads were washed twice with PBS and used directly for precipitation experiments.

Fluorescence and circular dichroism spectroscopy. The temperature dependence of protein fluorescence was determined as previously described[48]. The RGS protein samples (10 µM in PBS with 1 mM DTT) were excited at 280 nm (slit widths of 2 nm). Unfolding temperatures (T_u) were determined as the temperatures at which the derivative of the melting curve approached zero.

For circular dichroism (CD) spectroscopy, RGS proteins were buffer-exchanged into a buffer containing 20 mM phosphatase, pH 7.4, 80 mM NaF and 0.5 mM TCEP. CD spectra were measured with a Jacso J-810 Spectropolarimeter integrated with a Peltier temperature controller on 10 µM RGS in a 1-mm quartz cuvette (Hellma). Spectra were collected between 190 nm and 270 nm with 1-nm steps and from 10 °C to 90 °C with 10 °C steps. Every spectrum is an average of five acquisitions. SigmaPlot software was used to smooth the data.

Protein precipitation and western blotting. For comparison of protein expression levels, 100 ng of Axin plasmid DNA was transfected in a single well of a 24-well plate, unless otherwise indicated. For interaction of Axin RGS variants with APC, 30 µl GST-APC-SAMP2–bound beads was washed with 50 mM Tris, pH 7.4, 150 mM NaCl, 10% glycerol, 0.1% Triton X-100, 0.1% BSA, 1 mM EDTA and protease inhibitors, and incubated overnight with 0.5 ml of 2.6 µM RGS protein at 4 °C, with rotation. After being washed, beads were eluted with sample buffer and heating for 5 min at 100 °C. After SDS-PAGE was performed, protein bands were detected via staining with Coomassie brilliant blue R-250 or via western blotting onto PVDF membranes. After blocking with Odyssey blocking buffer (LI-COR), Axin variants were detected with goat anti-Axin (R&D systems, AF3287) and donkey anti-goat Alexa680 (Invitrogen, A21084). Other antibodies used for western blotting were anti-V5 (Genscript, A01724) and mouse anti-Actin (MP Biomedicals, 691001), which were detected with the secondary antibody goat anti-mouse-Alexa 680 (Invitrogen, A21058) and an Odyssey Infrared Imaging System (LI-COR). For all primary antibodies, validation is provided on the manufacturers' websites.

SDS-solubility analysis. HEK293T cells were grown in six-well plates and transfected with FuGene 6 (Promega) with the following constructs: 50 ng Axin-V5 WT or 100 ng Axin-V5 L106R, brought up to 1 µg with empty vector. Cells were lysed 24 h after transfection with SDS lysis buffer (50 mM Tris, pH 7.4, 100 mM NaCl, 5 mM EDTA, 0.5% Triton X-100, 1% SDS and protease inhibitors). Cells were lysed on ice, and this was followed by sonication to disrupt contaminating DNA. Lysates were cleared by centrifugation for 30 min at 4 °C (12,000 r.p.m.; Eppendorf 5415R). Supernatant (SDS-soluble fraction) was transferred to clean tubes and substituted with SDS sample buffer. Pellets were dissolved in 50 µl of 100% formic acid and air dried before being dissolved in 1× SDS sample buffer. Samples were analyzed with western blotting as described above.

Gene targeting and editing of the *Axn* locus. To compare the activity of Axin L67P, Axin V72R and Axin V72R I169R L170R, the corresponding cDNAs were reintegrated in an *Axn* KO allele generated with a targeting vector and protocol described previously[35]. Primers used for the amplification of homology arms were 5′-GACTGCGGCCGCGTCTCGGAGAGGAGCAACAGTTGAC-3′ (fw, 5′ arm) and 5′-ATCGGTACCCTTCCCACGACAAGCGATCGCTGC-3′ (rev, 5′ arm); and 5′-CATACTAGTGACCTCCTGGGTAAGTCAGCTCAGC-3′ (fw, 3′ arm) and 5′-AATGGCGCGCCTGGTCGCTGCTGGACTGATCGAGC-3′ (rev, 3′ arm). Primers for confirmation of 5′ recombination were 5′-ACTACG ATTGCATGCGAGAATCTCAG-3′ (genomic, fw) and 5′-CCAACTGAGAGA ACTCAAAGGTTACC-3′ (vector, rev). Primers for confirmation of 3′ recombination were 5′-GCTTATTCAGAAGCTTATCGATACCGTCGAC-3′ (vector, fw) and 5′-ATCAATCGATCGACCTCGTCCGTTC-3′ (genomic, rev). After confirmation of targeting into *Axn*, much of the targeting vector was removed by crossing to a strain expressing Cre constitutively (Bloomington stock 851), in a procedure outlined previously[35]. The resulting strain, referred to as *Axn*[KO], was used as a host for reintegration of various constructs via the *attP* site. Reintegration was achieved by injection into *Axn*[KO] embryos expressing the

PhiC31 integrase. Genotypes were as follows: Axin WT: *engrailed-Gal4, UAS-FLP/+; FRT82B Axn*[KI, wt]/*FRT82B ubi-GFP*, where 'KI, wt' indicates knock-in of the WT cDNA. For Axin-mutant strains, the *FRT82B Axn*[KI, wt] chromosome was replaced with *FRT82B Axn*[KI, L67P], *FRT82B Axn*[KI, V72R], *FRT82B Axn*[KI, V72R, I169R, L170R], or *FRT82B Axn*[KI, V72R, Y86R, F87R].

Immunofluorescence and confocal microscopy. HEK293T cells were grown on glass coverslips in 24-well plates (coated with laminin). After overnight transfection of 30 ng of Axin per well, cells were either fixed in ice-cold methanol or in 4% paraformaldehyde (PFA) in 50 mM sodium phosphate, pH 7.4, buffer. After being quenched in 50 mM NH_4Cl and blocked with 2% BSA and 0.1% saponin in PBS, cells were incubated with the primary antibody rabbit anti-V5 (Sigma, V8137) and then with the secondary antibody goat anti-rabbit Alexa568 (Molecular Probes, A11036). Cells were mounted in Prolong Gold with DAPI (Invitrogen, P36931). Images were acquired with a Zeiss LSM-510 confocal microscope and analyzed with ImageJ (http://imagej.nih.gov/ij/). The following antibodies were used: rabbit anti-V5 (Sigma, V8137), mouse anti-V5 (Genscript, A01724), rabbit anti-vimentin (Cell Signaling, 5741), rabbit anti-HDAC6 (Cell Signaling, 7558), mouse anti–γ-tubulin (Sigma, T5326), goat anti-rabbit Alexa568 (Molecular Probes, A11036), and goat anti-mouse Alexa488 (Molecular Probes, A11029). For all primary antibodies, validation is provided on the manufacturers' websites. CFTR-ΔF508 aggresomes were induced as described previously[29].

For wing imaginal discs, the following primary antibodies were used: guinea pig anti-Sens (a gift from H. Bellen, Baylor College of Medicine[49]) and mouse anti-Dll (gift from I. Duncan and D. Duncan, Washington University[50]). Alexa-conjugated anti-guinea pig (Molecular Probes, A21435) or anti-mouse (Molecular Probes, A10037) were used as the secondary antibodies. Imaginal discs were mounted in Vectashield (Vector Laboratories), and Z stacks were acquired with a Leica SP5 confocal microscope. Projections along the Z axis were rebuilt starting from 35–55 Z stacks with ImageJ.

NMR spectroscopy. Samples for NMR measurements contained 0.1 mM protein in 20 mM sodium phosphate, pH 6.5, 150 mM NaCl and 1 mM DTT with 10% ^2H_2O added for the lock signal. ^1H-^{15}N HSQC NMR spectra were recorded at 298 K on an Avance 600 Bruker NMR spectrometer equipped with a cryogenic triple-resonance gradient probe. All spectra were recorded with a recycle delay of 1.0 s, spectral widths of 20/30 p.p.m. centered at 4.7/118.5 p.p.m. in $^1H/^{15}N$, with 1,024 and 128 points, respectively, and 64 scans per increment. Spectra were processed with NMRPipe/Draw and analyzed with Sparky 3 (http://www.cgl.ucsf.edu/home/sparky/). Residues in the intrinsically disordered region of RGS Axin-1 (residues 2–220) were tentatively assigned on the basis of a comparison of the recorded NMR spectra with NMR spectra published for an Axin-1 construct containing only the RGS domain (residues 88–211)[18].

Small-angle X-ray scattering (SAXS) experiments. All experiments were carried out for purified proteins in 20 mM sodium phosphate, pH 6.5, 150 mM NaCl and 1 mM DTT at 298 K. SAXS data from solutions of WT, L101P and L106R Axin RGS domains were collected at the X33 beamline of the European Molecular Biology Laboratory (EMBL) Deutsches Elektronen Synchrotron (DESY) with a MAR345 image plate detector. Data were collected at 25 °C. The scattering patterns were measured with a 2-min exposure time (eight frames, each 15 s) for several solute concentrations in the range of 0.5 to 2.0 mg/ml. To assess radiation damage, the individual frames of the 2-min exposure were compared, and no changes were detected. With a sample-detector distance of 2.7 m, a range of momentum transfer of $0.01 < s < 0.6$ Å^{-1} was covered ($s = 4\pi \sin(\theta)/\lambda$, where 2θ is the scattering angle, and $\lambda = 1.5$ Å is the X-ray wavelength). SAXS data of WT, L106R and L106R F119R Axin RGS were also recorded on an in-house SAXS instrument (SAXSess mc2, Anton Paar) equipped with a Kratky camera, a sealed X-ray-tube source and a two-dimensional Princeton Instruments PI·SCX:4300 CCD detector (Roper Scientific). The scattering patterns were measured with a 90-min exposure time (540 frames, each 10 s) for several solute concentrations in the range of 0.5 to 2 mg/ml. Radiation damage was excluded on the basis of a comparison of individual frames of the 90-min exposures, where no changes were detected. A range of momentum transfer of $0.012 < s < 0.63$ Å^{-1} was covered ($s = 4\pi \sin(\theta)/\lambda$, where 2θ is the scattering angle, and $\lambda = 1.5$ Å is the X-ray wavelength). All SAXS data were analyzed with standard techniques implemented in the package ATSAS and SAXSQuant (version 3.9, for in-house scattering data). In-house scattering data were desmeared with GNOM and GIFT[51,52]. The forward scattering, I(0), and the radius of gyration, R_g, were evaluated with the Guinier approximation[53], assuming that at very small angles ($s < 1.3/R_g$), the intensity is represented as $I(s) = I(0)\exp((-s^2R_g^2)/3)$. The values of I(0) and R_g, as well as the maximum dimension, D_{max}, and the interatomic distance distribution functions, (P(R)), were also computed with GNOM[52]. The scattering from the high-resolution models was computed with CRYSOL[54]. The masses of the solutes were evaluated by comparison of the forward scattering intensity with that from a bovine serum albumin reference solution (mass of 66 kDa).

Size-exclusion chromatography. SEC experiments of WT and mutant RGS were performed on a HiLoad Sepharose 16/600 pg75 column (GE Healthcare). Oligomer peaks were eluted at ~50-ml retention volume for RGS L106R and RGS L106R F119R (fractions eluting from 45.0 to 52.5 ml), and monomer peaks were eluted at ~58-ml retention volume of RGS WT and RGS L106R F119R (fractions eluting from 52.5 to 61.5 ml). The maximal concentration within the monomeric RGS peak was 20 μM.

Analytical ultracentrifugation. AUC sedimentation velocity experiments were performed on SEC oligomer peaks on a Beckman ProteomeLab XL-A analytical ultracentrifuge (Beckman) at RT. Sedimentation velocity experiments of WT, L106R and L106R F119R Axin RGS were performed for sample concentrations of 0.23 g/L in a buffer of 50 mM Tris, pH 8, 500 mM NaCl and 2 mM β-mercaptoethanol at 42,000 r.p.m. at 20 °C. The protein was detected by an absorbance optics system at a wavelength of 280 nm. Scans were recorded every 6 min. A monomer peak was observed at a sedimentation coefficient of 2 S, and oligomeric species ranged from 8 to 100 S. Larger aggregates may have formed because of the higher protein concentrations (>2 g/L) occurring during the sedimentation process. Data analysis to determine the contributions of different species was performed with the C(s)-analysis module of the UltraScan software package[55]. dc/dt plots for graphical comparison of different samples were generated with Sedview[56].

Sample preparation for LC-MS/MS. Immunoprecipitated proteins on beads were resuspended in a spin filter column and washed three times with 200 μl of PBS to remove residual detergent from the lysis buffer. Bound proteins were then eluted off the beads first with 100 μl of 0.5% RapiGest SF (Waters) and then with 100 μl of 8 M urea, both dissolved in 50 mM ammonium bicarbonate, pH 8.0. Eluted proteins were reduced with 1 mM dithiothreitol (DTT) and alkylated with 5.5 mM iodoacetamide. For tryptic digestion, proteins were first digested with endoproteinase Lys-C (Wako Chemicals) at room temperature for 4 h; this was followed by digestion with sequencing-grade modified trypsin (Promega) overnight after four-fold dilution with 50 mM ammonium bicarbonate. Protease digestion was stopped by addition of trifluoroacetic acid (TFA) to a final concentration of 1%, and any precipitates were removed by centrifugation. Peptides were desalted with reversed-phase Sep-Pak C18 cartridges (Waters), dried and stored at −20 °C before LC-MS/MS.

Mass spectrometry. For LC-MS/MS analysis, peptides were first separated with a C18 column (Zorbax, Agilent) and introduced by nanoelectrospray into the LTQ Orbitrap Elite (Thermo Fisher) and MS/MS in data-dependent decision-tree mode (CID/ETD) as previously described[57].

MS data analysis. Raw data files were analyzed with Proteome Discoverer (version 1.3). The top ten most intense MS2 peaks were selected within every 100-Da bin and searched against the UniProt Human database (version 2013-07; 20,277 entries) with the MASCOT search engine. Trypsin/P was chosen, cysteine carbamidomethylation was set as a fixed modification, and oxidation of methionine and acetylation of the N terminus were set as variable modifications. Peptide tolerance was set to 15 p.p.m., and MS/MS tolerance was set to 0.5 Da. All peptide-spectrum matches (PSMs) and proteins were validated with 1% FDR. Finally, to rank and score individual protein-protein interactions, we used workflow 3 from the CRAPome software (http://crapome.org/)[58]. The default settings were chosen for all analyses except for the following parameters of the SAINT probability score[59], where we used n-burn = 2000; n-iter = 10,000; LowMode = 0; MinFold = 1 and Normalize = 1. To access changes in the interactome, each prey was assigned a probability score for interaction (SAINT score) ranging from

doi:10.1038/nsmb.3191

0.0 to 1.0. Higher SAINT scores indicated a higher confidence of the prey being a genuine interactor of Axin1, in comparison to negative-control IPs. Low SAINT scores indicated that the candidate was a background contaminant. On the basis of the pattern of SAINT-score distribution among the different Axin1 isoforms, each putative interactor was further clustered into four clusters: 'unaffected', 'lost', 'trapping rescued' and 'loss rescued'. We classified proteins with at least a 0.9 binding probability (SAINT score ≥0.9) as unaffected. These data form the basis of **Figure 4f** and **Supplementary Figure 5** (with STRING v10). The full MS proteomics data have been deposited in the ProteomeXchange Consortium[60] via the PRIDE partner repository under data set identifier PXD003116.

45. Willert, K. *et al.* Wnt proteins are lipid-modified and can act as stem cell growth factors. *Nature* **423**, 448–452 (2003).
46. Tauriello, D.V. *et al.* Loss of the tumor suppressor CYLD enhances Wnt/beta-catenin signaling through K63-linked ubiquitination of Dvl. *Mol. Cell* **37**, 607–619 (2010).
47. Cabrita, L.D. *et al.* Enhancing the stability and solubility of TEV protease using *in silico* design. *Protein Sci.* **16**, 2360–2367 (2007).
48. Rudiger, S., Freund, S.M., Veprintsev, D.B. & Fersht, A.R. CRINEPT-TROSY NMR reveals p53 core domain bound in an unfolded form to the chaperone Hsp90. *Proc. Natl. Acad. Sci. USA* **99**, 11085–11090 (2002).
49. Nolo, R., Abbott, L.A. & Bellen, H.J. Senseless, a Zn finger transcription factor, is necessary and sufficient for sensory organ development in *Drosophila*. *Cell* **102**, 349–362 (2000).
50. Duncan, D.M., Burgess, E.A. & Duncan, I. Control of distal antennal identity and tarsal development in *Drosophila* by spineless-aristapedia, a homolog of the mammalian dioxin receptor. *Genes Dev.* **12**, 1290–1303 (1998).
51. Bergmann, A., Fritz, G. & Glatter, O. Solving the generalized indirect Fourier transformation (GIFT) by Boltzmann simplex simulated annealing (BSSA). *J. Appl. Crystallogr.* **33**, 1212–1216 (2000).
52. Svergun, D.I. Determination of the regularization parameter in indirect-transform methods using perceptual criteria. *J. Appl. Crystallogr.* **25**, 495–503 (1992).
53. Guinier, A. La diffraction des rayons X aux très petits angles: application à l'étude de phénomènes ultramicroscopiques. *Ann. Phys.* **12**, 161–237 (1939).
54. Svergun, D., Barberato, C. & Koch, M.H.J. CRYSOL: a program to evaluate X-ray solution scattering of biological macromolecules from atomic coordinates. *J. Appl. Crystallogr.* **28**, 768–773 (1995).
55. Demeler, B., Brookes, E. & Nagel-Steger, L. Analysis of heterogeneity in molecular weight and shape by analytical ultracentrifugation using parallel distributed computing. *Methods Enzymol.* **454**, 87–113 (2009).
56. Hayes, D.B. & Stafford, W.F. SEDVIEW: real-time sedimentation analysis. *Macromol. Biosci.* **10**, 731–735 (2010).
57. Frese, C.K. *et al.* Improved peptide identification by targeted fragmentation using CID, HCD and ETD on an LTQ-Orbitrap Velos. *J. Proteome Res.* **10**, 2377–2388 (2011).
58. Mellacheruvu, D. *et al.* The CRAPome: a contaminant repository for affinity purification-mass spectrometry data. *Nat. Methods* **10**, 730–736 (2013).
59. Choi, H. *et al.* SAINT: probabilistic scoring of affinity purification–mass spectrometry data. *Nat. Methods* **8**, 70–73 (2011).
60. Vizcaíno, J.A. *et al.* ProteomeXchange provides globally coordinated proteomics data submission and dissemination. *Nat. Biotechnol.* **32**, 223–226 (2014).